Nonradiating Resonances: Anapoles Enabling Highly Efficient Plasma Jets Within Dielectric Structures

Muhammad Rizwan Akram, *Member, IEEE*, and Abbas Semnani, *Senior Member, IEEE*

***Abstract*— Plasma plays a pivotal role in numerous applications. When plasma interacts with air, it creates rare and highly reactive species. Typically, the generation of atmospheric air plasma jets relies on resonant cavities to enhance plasma efficiency. In this study, we have harnessed the innovative concept of nonradiating sources, known as anapoles, which utilize the lowest order multipoles—specifically, electric–electric dipole interactions—within a hybrid metallodielectric structure. This approach enhances the near electric field, facilitating gas breakdown for the realization of a plasma jet. The achievement of a dielectric plasma jet is remarkable in its own right, particularly when considering the open structure employed, which enables frequency tuning. Furthermore, the demonstrated prototype surpasses the existing plasma jets in several key aspects, including compactness, compatibility with planar fabrication techniques, power efficiency, cost-effectiveness, tunability, and electron density. With these substantial enhancements, the proposed technique can substantially enhance plasma jet technology and open exciting avenues for exploring novel applications.**

***Index Terms*— Anapoles, dielectric resonator, frequency tunable, plasma jet, power efficiency.**

I. Introduction

THE confinement of electromagnetic (EM) waves or light [1], [2] within metamaterial structures on a subwavelength scale has emerged as a crucial platform for exploring fundamental wave–matter interactions [3], [4], [5] and a wide range of applications, particularly in wireless [6] and optical domains [7], [8]. In wireless applications, such as sensing [9], filtering [10], and energy transfer [6], achieving high-quality wave confinement within resonating structures is paramount. Consequently, novel concepts, such as "bound states in the continuum" [1], [11] and "anapoles" [12], [13], have garnered significant attention for enhancing wave confinement and providing high-Q resonances. However, due to the nonexistence theorem [1], perfect bound states in a continuum cannot be realized in isolated structures. Conversely, anapoles [14] represent charge-current configurations that can be achieved through external excitation, inducing multipole moments within the structure that produce equal but out-of-phase far-field radiation.

The initial demonstration of anapoles harnessed the interference between electric and magnetic dipoles, primarily focusing on toroidal dipoles, as a means to minimize outgoing scattering. Subsequently, anapoles have evolved beyond the confines of toroidal dipoles and have been realized through various combinations of other multipole configurations [6], [15]. This versatility has prompted extensive exploration within the context of plane wave scenarios [16], [17]. More recently, there has been a concerted effort to achieve dipole-like excitation of anapoles, a development that holds promise for more compact devices [6], [18], [19]. However, a significant challenge lies in the requirement for high dielectric constant materials, which has posed a substantial barrier to practical applications. In our prior work [20], we successfully demonstrated a compact anapole technology utilizing the lowest order electric dipoles in conjunction with readily available, low-dielectric-constant materials. This breakthrough opens the door to developing wireless applications that leverage anapole technology.

While anapole sources are energy storage devices, their storage capacity is inherently constrained by the materials used in their construction. This limitation prompts us to consider the potential applications of anapoles. In the context of our work, we have envisioned their application in developing efficient plasma sources. The augmented electric field generated by the presence of anapoles has the potential to initiate gas breakdown at much lower powers than usual, enabling the creation of efficient plasma sources. Plasma, the fourth state of matter, is pivotal in diverse fields, including medicine [21], materials processing [22], agriculture [23], and space applications [24]. Given its profound impact across various aspects of daily life, developing efficient plasma sources is paramount.

High-frequency-driven plasmas have recently garnered attention due to their operation in the α-discharge regime [25], [26], characterized by a low sheath voltage, which complements plasma discharge stability while addressing the significant issue of electrode erosion that affects the device's lifespan. High-frequency plasmas employ two main approaches. Nonresonant sources [27], while effective, tend to be bulky and demand substantial power, giving rise to safety and EM interference concerns. In contrast, resonant plasma sources (RPSs) offer an appealing alternative. In RPS, EM energy is concentrated at specific spatial locations within resonant structures, creating favorable conditions for gas breakdown and

Manuscript received 24 May 2024; revised 12 July 2024 and 6 August 2024; accepted 10 August 2024. Date of publication 23 August 2024; date of current version 7 January 2025. This work was supported by the National Science Foundation (NSF) under Grant ECCS-2102100. *(Corresponding author: Muhammad Rizwan Akram.)*

The authors are with the Department of Electrical Engineering and Computer Science, The University of Toledo, Toledo, OH 43606 USA (e-mail: muhammadrizwan.akram@utoledo.edu; abbas.semnani@utoledo.edu).

Color versions of one or more figures in this article are available at https://doi.org/10.1109/TMTT.2024.3443716.

Digital Object Identifier 10.1109/TMTT.2024.3443716

plasma formation. These RPS exhibit a range of advantageous features, including stable discharges, a higher degree of ionization and dissociation, elevated electron density, increased production of reactive species, lower plasma discharge temperatures, and reduced ignition voltage. Various solutions, such as the shorted waveguides [28], [29], cavity resonators [30], [31], [32], and microstrip split ring resonators [33], have been proposed as plasma sources, showcasing the versatility of this approach.

Although RPSs are very favorable as plasma generators operate at very low power, these suffer severely because of impedance mismatch before and after plasma ignition. For example, evanescent mode cavity resonator (EVA)-based [34] atmospheric pressure microwave plasma jet can operate at low power of 500 mW, and coaxial transmission line resonators-based [35] plasma jet can operate at 1.5–3 W. Moreover, recently, substrate-integrated waveguide-based cavity resonator [36] and EVA resonator [37] have been proposed for printed circuit board (PCB) compatibility. These require slightly higher power for plasma ignition, i.e., 15–30 W for cavity resonators and 2.7–5 W for EVA resonators. However, their performance drastically suffers owing to the presence of conductive plasma volume in the narrow gap, typically in the micrometer range for the high electric field as desired for plasma ignition.

This study introduces a novel approach for developing highly efficient atmospheric plasma jets with minimal reflection and radiation losses using dielectric anapole structures. Unlike commonly employed cavity resonators, anapoles do not necessitate a metallic enclosure for radiation mitigation. The anapole structure designed for the plasma jet application leverages only the lowest order electric dipoles induced on both the metallic and dielectric components of the device to minimize radiation losses through the destructive interference of outgoing waves. The proposed device is planar, exceptionally compact, and seamlessly integrates with PCB structures. Its cost-effectiveness is owed to its compatibility with PCB fabrication processes. Furthermore, the resulting plasma jet exhibits remarkable coupling efficiency, reaching as high as 94% at a low input power of 1.5 W and 62% at a high input power of 15 W. The anapoles plasma jet offers double the electron density compared with state-of-the-art waveguide/cavity-based resonant microwave plasma jets despite requiring any metallic enclosures.

II. Anapole Plasma Jet Theory and Design

The hybrid metallodielectric structure shown in Fig. 1 is employed to realize the anapole device. The introduced anapole configuration combines two resonances to nullify far-field radiation without necessitating metallic enclosures. This achievement was attained by harnessing the $HE_{11\delta}$ mode of a cylindrical dielectric resonator antenna perturbed by an embedded loop. These resonances effectively counteract far-field emissions. The anapole working mechanism is the opposite of antennas, as radiation suppression is the main goal for anapoles. The radiation suppression in the proposed anapole device is achieved with the excitation of the lowest order multipoles, i.e., electric dipoles over the metallic and

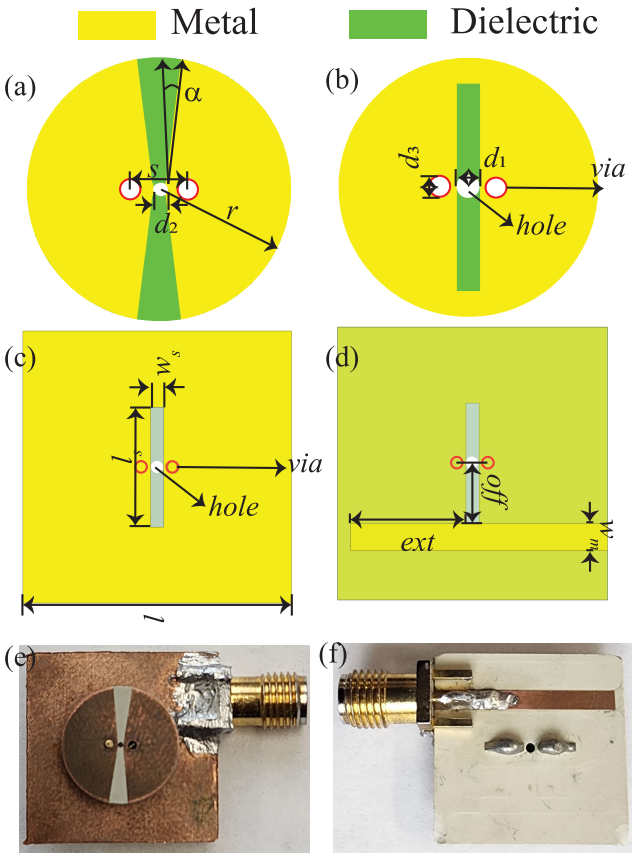

Fig. 1. (a) and (c) Top and (b) and (d) bottom views of the dielectric resonator and the feeding board of the anapole device with $r = 11$ mm, thickness of the dielectric cylinder $h = 3.81$ mm, and thickness of feed board $h_2 = 1.27$ mm, $l_s = 8.83$ mm, $l = 20$ mm, $w_m = 2$ mm, ext $= 9$ mm, off $= 5.3$ mm, $w_s = 1$ mm, $d_1 = 1$ mm, $d_2 = 0.5$ mm, $d_3 = 0.9$ mm, and $s = 1.2$ mm. The cylindrical resonator is made of TMM13i with a permittivity of $\epsilon_r = 13$ and $\tan\delta = 1.9 \times 10^{-3}$. The bottom board is made of TMM6 with a permittivity of $\epsilon_r = 6$ and $\tan\delta = 2.3 \times 10^{-3}$. The fabricated anapole plasma jet device: (e) top view and (f) bottom view.

dielectric parts. The induced electric dipoles on both the metallic and dielectric components are strategically aligned to effectively cancel out far-field radiation while simultaneously enhancing the concentration of the near field. This interaction results in a substantial increase in the electric field strength in the vicinity of the device, which is used for gas breakdown.

The Cartesian multipole expansion is employed to evaluate the strength of electric and magnetic dipole, quadrupole, and toroidal dipole and their contribution to the far-field radiation over the proposed anapole device, as shown in Fig. 2. This is done by integrating the current density within the dielectric volume and on the metallic parts through the postprocessing options available in COMSOL Multiphysics. The involved Cartesian multipoles are defined as follows [38]:

$$p_i = \frac{1}{iw}\int J_i dv \tag{1}$$

$$m_j = \frac{1}{2}\int (\boldsymbol{r} \times \boldsymbol{J})_j dv \tag{2}$$

$$Q^e_{ij} = \frac{1}{iw}\int (r_j J_i + r_i J_j + \frac{2}{3}\delta_{ij}(\boldsymbol{r}.\boldsymbol{J}))dv \tag{3}$$

$$Q_{ij}^{m} = \frac{1}{3}\int ((\boldsymbol{r}\times\boldsymbol{J})_i r_j + (\boldsymbol{r}\times\boldsymbol{J})_j r_i)dv \tag{4}$$

$$T_i^{e} = \frac{1}{10}\int ((\boldsymbol{r}.\boldsymbol{J})r_i - 2r^2 J_i)dv. \tag{5}$$

Here, subscripts i, $j = x$, y, and z; superscripts e and m are electric and magnetic, respectively; and symbols p, m, Q, and T represent electric dipole, magnetic dipole, quadrupole, and toroidal, respectively. $\boldsymbol{J}$ is the total of surface current and induced currents inside the device

$$\boldsymbol{J} = iw\epsilon_0(\epsilon_r - 1)\boldsymbol{E} \tag{6}$$

where ω is the angular frequency, ϵ_0 is the vacuum permittivity, ϵ_r is the relative permittivity of the dielectric, and E is the electric field. The total radiation intensity of these multipoles can then be calculated using

$$I_{\text{Total}} = \frac{k^4}{12\pi\epsilon_0^2 c\mu_0}\left|\boldsymbol{p} - \frac{ik}{c}\boldsymbol{T^e}\right|^2 + \frac{k^4}{12\pi\epsilon_0 c}|\boldsymbol{m}|^2 + \frac{k^6}{160\pi\epsilon_0^2 c\mu_0}|\boldsymbol{Q^e}|^2 + \frac{k^6}{160\pi\epsilon_0 c}|\boldsymbol{Q^m}|^2. \tag{7}$$

The overall radiation is around 190 mW out of 1 W, mainly contributed by electric dipoles. To analyze the underlying mechanism, the electric dipole strength is separately evaluated over metallic and dielectric parts. Only the $x-$ aligned component is dominant, which is 180° out of phase between metallic and dielectric parts, resulting in radiation suppression. Further details on complete radiation suppression are provided in our previous work [20]. It is important to note that the radiation intensity calculated through (7), as denoted by a sum in Fig. 2, is in complete agreement with the COMSOL simulated radiation, validating the Cartesian multipole expansion method results.

Another validation can be observed for electric field plots in Fig. 3, which is consistent with the multipoles approach. The electric field is plotted on the XY plane inside the dielectric disk at two different phase values, as shown in Fig. 3. The phase values of 30° and 170° are utilized for better visualization, as these correspond to $+x$ and $-x$ peaks of the E-field. It can be verified that the solid red arrows correspond to the electric dipole aligned along the x-direction, excited in the loop that is formed by the vias. The relatively weaker x-aligned electric dipole is excited by the dielectric disk. At any phase, these are directed in opposite directions, indicating antiphase as illustrated conceptually in Fig. 3. The electric field plots agree well with the Cartesian multipole evaluations, where x-directed electric dipoles are antiphase in metallic and dielectric parts. Moreover, the unequal strength of the two dipoles results in radiation leakage, which we will refer to as radiation loss. Leveraging the insights gained, the anapole structure was optimized to realize an efficient atmospheric pressure plasma jet operating at 2.45 GHz.

The designed anapole structure consists of two separate boards: a cylindrical dielectric disk and a feeding microstrip board. The cylindrical disk is intricately fashioned from a commercially available Rogers TMM13i laminate, possessing a thickness of 3.81 mm and a 35-μm copper cladding. This disk serves as the resonant element of the anapole plasma jet and

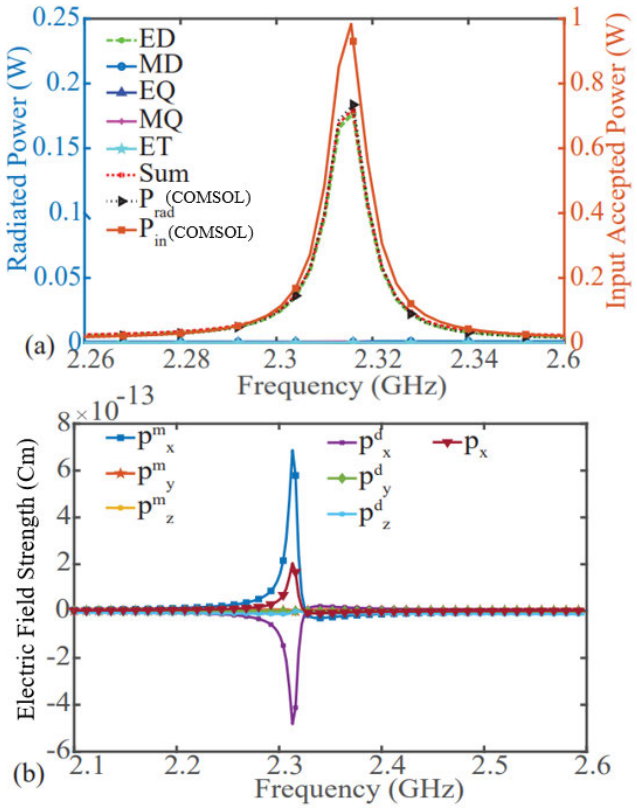

Fig. 2. (a) Radiation assessment for various dipoles, where ED stands for electric dipole, MD for magnetic dipole, EQ for electric quadruple, MQ for magnetic quadruple, ET for electric toroidal dipole, and sum is the total contribution of all multipoles. P_{rad} and P_{in} denote the simulated values of radiated and accepted power by anapole, with only the P_{in} scale corresponding to the orange color. (b) Evaluation of electric dipole (p) strength over metallic and dielectric components, where superscripts m and d correspond to metallic and dielectric parts, respectively. The polarizations are denoted by x, y, and z.

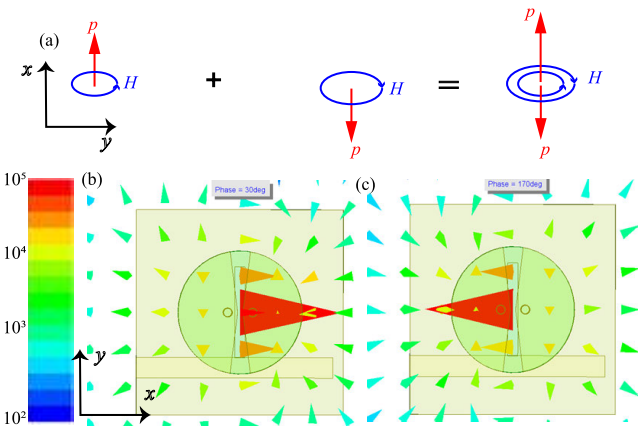

Fig. 3. (a) Conceptual illustration of out-of-phase dipoles and electric field plot over XY plane passing through the middle of the cylindrical disk at (b) 30° phase and (c) 170° phase.

incorporates vias to create a split-ring resonator configuration. A rectangular slot is also etched into the disk's bottom layer to enable EM energy coupling from the feeding network to the dielectric resonator cavity. For the feeding board, another layer is fabricated from a 1.27-mm-thick Rogers TMM6 laminate featuring the same 35-μm cladding with a 50-Ω microstrip line on the bottom side and a slot of identical dimensions on the top. The positionings of the microstrip line, slot width (w_s), and length (l_s) have been meticulously optimized to achieve

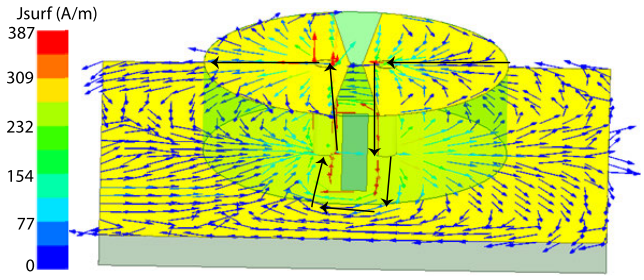

Fig. 4. Vector current plot over the anapole device.

excellent impedance matching at the resonant frequency of 2.45 GHz. The assembly process involves aligning the cylindrical disk with the feeding board using vias and metallic rods, which are then securely affixed using silver epoxy.

The compactness of the proposed anapole device primarily stems from its exclusive utilization of the lowest order electric dipoles. This characteristic facilitates a compact form factor, even when operating with a low dielectric constant, for example, $\epsilon_r = 12.85$ in this design, as opposed to prior anapole investigations, which typically employed dielectric constants in the range of 1000 [6], [19]. In addition, the device achieves enhanced compactness by incorporating elongated current paths (enhancing the electrical size to lower the frequency), illustrated in Fig. 4, by integrating copper patterns atop its structure similar to the dielectric antenna miniaturization techniques. Consequently, the overall dimensions amount to merely $0.33\lambda_g$ compared with approximately $4\lambda_g$ in previous works [6], [18], [19], where λ_g is the wavelength in the dielectric medium, showing almost 12 times size reduction. Further enhancements in compactness are attained through the introduction of frequency tunability, facilitated by external variable capacitors. Detailed design schematics and images of the fabricated device are provided in Fig. 1(a)–(f).

To establish the necessary gas flow mechanism for plasma jet formation, a 1-mm hole is drilled between the rods and extends to the center of the cylindrical disk. As it approaches the disk's surface, the hole is tapered down to a diameter of 0.5 mm. This final hole size ultimately determines the diameter of the plasma jet. A Teflon capillary tube is then threaded through this hole, extending from the feeding board to the midpoint of the disk. This capillary tube serves as the conduit for gas injection. Positioning the hole at the disk's center within the dielectric resonator cavity is a deliberate choice, ensuring a sufficiently strong electric field for facilitating plasma ignition, as illustrated in Fig. 5(b). Furthermore, the slot on the top side of the disk is tapered to minimize the risk of air breakdown at various points along its length.

III. Materials and Methods

The proposed anapole device is numerically evaluated using the high-frequency structure simulator (HFSS) 2023 R1, employing the eigenmode solver. This analysis yielded an estimated Q-factor reaching 256 at the design frequency of 2.45 GHz. Subsequently, the driven solution was used to assess the return loss near the resonance frequency, as illustrated in Fig. 5(a). The radiation loss was also determined, measuring 190 mW out of 1 W for the proposed plasma jet device. The

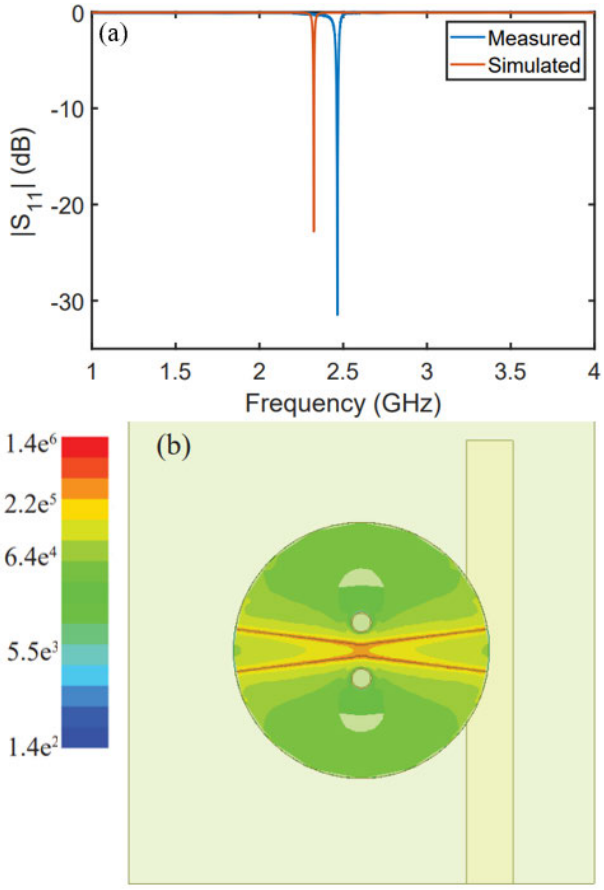

Fig. 5. (a) Simulated and measured reflection coefficients showcase a solid resonance. (b) Enhanced electric field in the range of 10^6 (V/m) at the gas ignition region.

proposed device consists of two distinct components: a cylindrical disk and a feeding board fabricated by PCB techniques. The cylindrical disk is crafted from Rogers TMM13i laminate and incorporates two vias and a central hole to prevent unintended air breakdown. The feeding board is constructed using Rogers TMM6 material. It is affixed to the disk using metallic rods of smaller dimensions than the vias, ensuring proper slot alignment. Silver epoxy is employed to fasten the disk atop the feeding board securely. Microwave energy is coupled to the device via a 50-Ω SMA connector.

After the sample preparation, a vector network analyzer (VNA) is employed to measure the scattering parameters, as depicted in Fig. 5(a). Parametric studies are performed for parameter off to enhance impedance matching, keeping the slot width $ws = 1$ mm, and parameter ws to optimize the operating frequency, keeping off $= 5.4$ mm, as shown in Fig. 6. The low radiation characteristics of the proposed anapole device make it well suited for plasma ignition without the need for an enclosed metallic cavity.

The setup for achieving plasma ignition is illustrated in Fig. 7. The signal generator N5181A generates a continuous wave (CW) signal at the resonance frequency, which is subsequently amplified by the AMP2070 power amplifier, providing approximately 57 dB of gain. The amplified signal passes through an isolator to safeguard the amplifier from back-reflected signals. Subsequently, the signal is routed through a

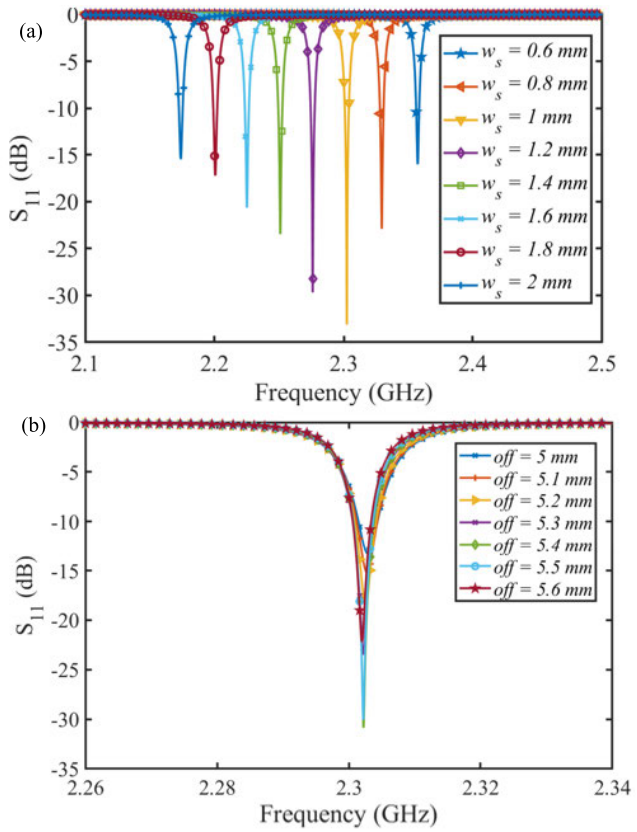

Fig. 6. Simulated reflection coefficients: (a) off = 5.4 mm and (b) w_s = 1 mm.

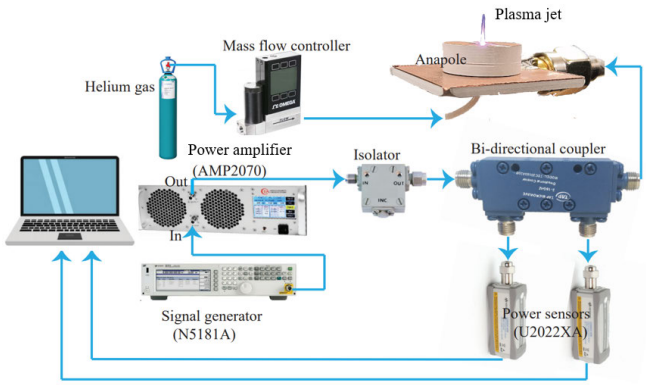

Fig. 7. Experimental setup for the anapole plasma jet ignition and characterization.

30-dB bidirectional coupler, where two power sensors, namely, U2022XA, are employed to measure the input and reflected powers. A compressed helium gas cylinder is connected to a mass flow controller (MFC), which regulates the gas flow rate directed to the device. For a gas flow rate of 1 slpm, plasma ignition is achieved at an input power of 2.7 W and can be sustained with an input power as low as 1 W.

The power sensors in the above setup are employed to measure the input and reflected powers at the terminal of the anapole device in the presence of the plasma jet using a bidirectional coupler

$$P_d = P_{\text{in}} - P_{\text{ref}} \tag{8}$$

$$\text{Power efficiency} = \frac{P_d}{P_{\text{in}}}. \tag{9}$$

To accurately measure the powers, it is necessary to account for the losses incurred by cables and components between the reflected port and the input port of the anapole device. These losses are determined prior to plasma ignition through a VNA measurement and are factored in for precise power measurements at the input port of the anapole device. The delivered power to the anapole plasma jet device can be readily derived from the reflected power, and the efficiency is subsequently calculated using the transmitted power and input power using (8) and (9). Assuming dielectric material with a low loss tangent of 0.0019 and a radiation loss of <20%, a significant portion of the delivered power to the device is indeed delivered to the plasma, especially considering the low ignition voltage compared with state-of-the-art metallic cavities. However, an advanced multiphysics simulation involving EMs, plasma, heat, and flow physics would be required to assess the actual power absorbed by the plasma for plasma power efficiency calculation.

We employed the Teledyne Princeton Instruments HRS-500-SS spectrometer, which offers an optical resolution of 0.05 nm, to assess the spectral emissions. The optical sensor was positioned near the device, approximately 1–2 mm away from the side, to prevent interference with the gas flow. This placement was optimized to capture the most comprehensive spectral profile of the desired emitter. To ensure data stability and minimize variations, the sensor's exposure time was set to 10 s, allowing adequate time for the data to stabilize.

IV. Results and Discussion

The frequency response of the proposed device was initially assessed in the OFF mode, employing both numerical simulations and experimental measurements, as illustrated in Fig. 5(a). Notably, the gas flow was found to have an insignificant impact on the resonance frequency and can, thus, be considered a nonsignificant factor in this context. In the experimental measurements, a slight shift of approximately 130 MHz in the resonance frequency is observed compared with the simulation results. This deviation can be attributed to the fabrication tolerances inherent to the manufacturing process, as the initial design had aimed for a resonance frequency of 2.45 GHz. Remarkably, the achieved return loss, surpassing 20 dB, underscores that over 99% of the input microwave energy is efficiently coupled to the anapole device at the resonant frequency.

To induce gas breakdown, it is crucial to establish a high electric field of around 10^5 (V/m) within the gas flow region. The electric field distribution was numerically evaluated in the proposed anapole design, utilizing an input power of 1 W, as illustrated in Fig. 5(b). Here, a maximum electric field strength of 1.4×10^6 (V/m) is observed, accompanied by a radiation loss of approximately 190 mW out of the 1-W input power. It is essential to mention that a potential strategy for reducing radiation loss involves employing a narrower slot on top of the disk without tapering. However, such an approach might increase the risk of undesired air breakdown, which is undesirable in the context of a plasma jet device. Furthermore, it is noteworthy that the peak electric field strength remains unaffected by the heightened radiation loss resulting from

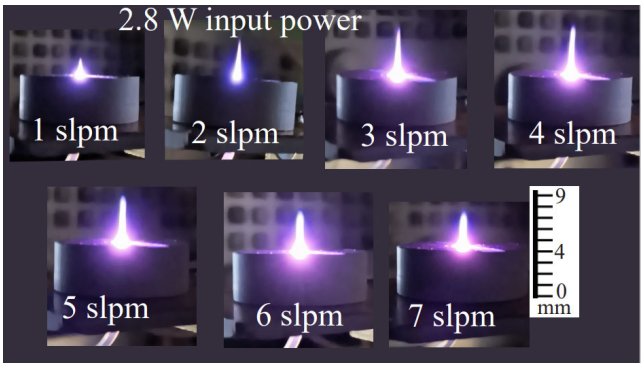

Fig. 8. Images of the anapole plasma jet at various helium flow rates at a constant input power of 2.8 W.

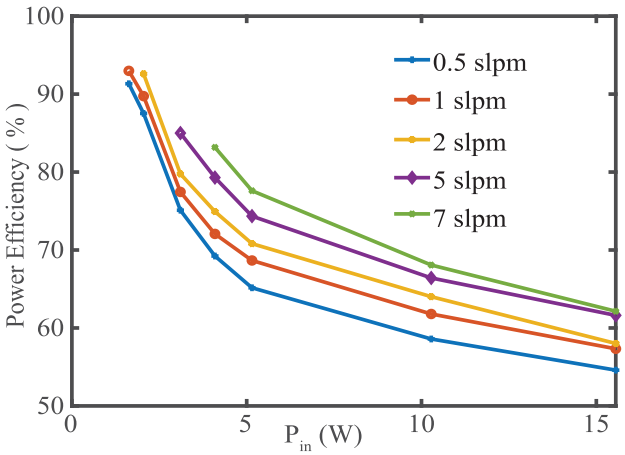

Fig. 9. Measured power efficiencies versus input power at various helium flow rates.

slot tapering. To further assess the safety of the device for commercial applications, the specific absorption rate (SAR) is evaluated using a three-layer model [39], [40] at the input power of 2.8 W, 5 cm in front of the device, and the SAR value of 1.9 W/Kg was obtained, which is below the permissible limit of 2 W/Kg for the European standard at such as close distance.

To test the device in ON mode, helium gas was introduced into the device at 1 slpm. At 2.7 W of input microwave power at the resonant frequency, gas breakdown occurred, forming a plasma jet. Due to the reduced effective area postbreakdown, even lower power in the 1-W range proved sufficient to sustain the plasma jet after ignition. To gain further insight into the characteristics of the plasma jet, the helium flow rate was varied, ranging from 1 to 7 slpm, and the resulting plasma jets are depicted in Fig. 8. Notably, the plasma jet length exhibited an increasing trend with a rising flow rate until it reached 5 slpm. At this point, an optimal plasma jet configuration was observed. Beyond this flow rate, the jet length began to decrease. The jet length directly corresponds to the nature of the gas flow, which can be estimated from the Reynolds number; the details can be found in [36]. The laminar flow is desirable for achieving a uniform plasma discharge, a characteristic that aligns well with the experimental observations presented in Fig. 8.

The plasma jet's efficiency is experimentally characterized. The device exhibits a reflection coefficient of approximately −20 dB in the OFF mode. However, when plasma ignites, it perturbs the frequency response due to the creation of a relatively conductive plasma region positioned directly within the high-field region of the structure. Due to plasma's conductive nature, perfect impedance matching is hindered upon plasma formation, diminishing the delivered power to the device and consequently reducing its efficiency. This phenomenon becomes particularly pronounced when utilizing high power levels to generate reactive species, as it expands the plasma volume. Experimental measurements are conducted to determine the input and reflected powers at various flow rates, enabling the calculation of the delivered power to the anapole device. Based on these numbers, the device's efficiency is calculated and depicted in Fig. 9. It is observed that the proposed anapole plasma jet consistently maintains a relatively low reflection, even at high operating powers. This characteristic highlights that the need for circulators and couplers can be circumvented without compromising the safety of the microwave sources, as is often required in the case of conventional resonant plasma jet sources.

The power efficiency of the proposed device is impressively high, reaching 94% at a low input power of 1.5 W and 62% at a higher input power of 15 W. This level of efficiency sets the proposed anapole device apart from earlier plasma jets, particularly those designed for low-power operation. For instance, the efficiency of the anapole device significantly surpasses that of the evanescent-mode cavity resonator-based plasma jet [34], which achieved 80% efficiency at 1-W input power and 18% efficiency at 15-W input power. Similarly, the proposed anapole device outperforms coaxial transmission line resonator-based plasma jets [35], which attain 80% efficiency at a low input power of 1.5 W. The comparison of the proposed technology with the literature is presented in Table I.

Critical parameters governing the usability of a plasma jet for various applications include gas temperature and electron density. To ensure the safety of the plasma jet, it is essential to maintain a temperature close to room level. In this context, the plasma discharge temperature was characterized by evaluating the rotational gas temperature for diatomic molecules N_2^+ [34]. To achieve this, optical emission spectroscopy (OES) was employed, utilizing a high-resolution optical sensor to capture the spectral profile of N_2^+ molecules over a 10-s duration. Subsequently, the experimentally obtained profile was compared with the spectrum generated by LIFBASE for N_2^+ molecules. The discharge temperature was accurately calculated with a ±5-K precision by comparing the two spectral profiles. As an illustration, for an input power of 15 W and a gas flow rate of 5 slpm, the experimental and simulated profiles are juxtaposed in Fig. 10(a), showcasing an excellent alignment between the two profiles at a temperature of 350 K. The gas temperature remains at 315 K for an input power of 5 W. It rises to 350 K at an input power of 15 W. This temperature range ensures the device's safety for temperature-sensitive applications, such as plasma medicine.

Determining the gas temperature makes it possible to characterize the electron density of the anapole plasma jet. To achieve this, OES is employed to analyze spectral profiles.

TABLE I
COMPARISON WITH THE STATE-OF-THE-ART PLASMA JET DEVICES

	$P_{in}(W)$	Electron Density (cm^{-3})	Technology/ Topology	Power Efficiency	PCB Compatibility	Compactness (λ)	Frequency tuning
[41]	2-10	10^{15}	CTL resonator	83%	No	0.25	No
[42]	88	10^{15}	CTL resonator	-	No	-	No
[34]	0.5	7.6×10^{15}	EVA resonator	80%	No	0.25	No
[36]	15-40	-	Cavity Resonator	-	Yes	0.54	No
[37]	2.7	10^{15}	SIW-EVA resonator	-	Yes	-	No
This work	1	1.5×10^{16}	Anapole	94%	Yes	0.05-0.09	1.6GHz - 2.5GHz

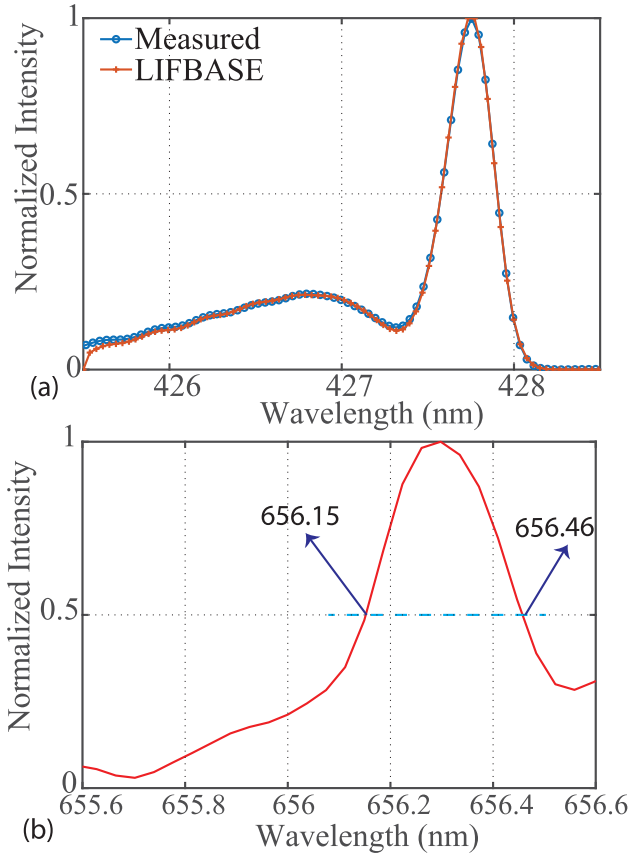

Fig. 10. (a) Excellent agreement between the simulated and measured spectral profiles at 5-slpm flow rate and 15-W input power for a temperature of 350 K. (b) H-α line at 15-W input power and 5 slpm of helium flow rate. $\Delta\lambda_{\text{Stark}}$ is calculated from FWHM as required to extract the jet electron density.

Among the commonly utilized spectral profiles in this context are the spectral emissions of hydrogen atoms, specifically Balmer alpha (H-α) at 656.279 nm and Balmer beta (H-β) at 486.135 nm, due to their visibility in the spectrum and distinct linear Stark effect. In this study, we opted to employ the H-α lines for estimating the electron density (n_e), as they offer more outstanding distinctiveness when compared with the H-β spectral profiles.

A spectral profile within the atmospheric plasma jet can be described as a convolution of Gaussian and Lorentzian profiles, collectively referred to as the Voigt function. The Gaussian component of the spectral profile is influenced by factors, such as the mass of the hydrogen atom, central wavelength, and gas temperature. Conversely, the Lorentzian component, which is more dominant, encompasses Doppler, van der Waals, and Stark broadening effects. It is important to note that resonance broadening due to interactions between neutral atoms of the same kind, while present, is typically negligible for Balmer lines at atmospheric pressure and can, therefore, be disregarded. The remaining three broadening mechanisms are accurately considered when assessing the electron density. Doppler broadening, for instance, arises when emitting atoms exhibit random motion, and the full-width at half-maximum (FWHM) can be determined as follows:

$$\Delta\lambda_D = \lambda_0\left(8\ln 2\frac{K_b T_g}{m_a c^2}\right). \tag{10}$$

Here, the gas temperature T_g is in kelvin, Boltzmann's constant K_b is in JK^{-1}, and m_a denotes the mass of the emitter. Van der Waals broadening, on the other hand, arises due to interactions between atoms of different species and can be estimated as follows:

$$\Delta\lambda_{vdW} = \frac{C}{T_g^{0.7}} \tag{11}$$

where C is a gas constant equal to 2.42 for helium.

The Doppler and van der Waals broadenings are calculated using the above formulas for a gas flow rate of 5 slpm under various input powers, as detailed in Table II, along with the corresponding measured temperatures. Furthermore, the FWHM of the H-α spectral line is determined from Fig. 10(b). It is noteworthy that $\Delta\lambda_D$ and $\Delta\lambda_{vdW}$ are found to be very small compared with the FWHM of H-α, indicating that Stark broadening is the dominant profile. Consequently, the electron density of the plasma jet is estimated using Stark broadening as follows:

$$n_e = 10^{17}\times(\Delta\lambda_{\text{Stark}}/1.098)^{1.47135}. \tag{12}$$

Here, n_e is in cm^{-3}, and λ_{Stark} is in nm. The evaluated n_e is approximately $1.55\times10^{16}\ \text{cm}^{-3}$, at least twice the values typically achieved in conventional plasma jets employing resonant cavity approaches. Repeated measurements were performed, and there was no visual effect of the plasma on the device, but the results were repeatable. The device works fine up to 100 W of power. However, with further power, the arcing (air ignition) could happen at the slot, which could slightly shift the frequency because of dielectric burning.

The interaction between a plasma jet and the surrounding ambient air holds significant potential for generating highly reactive species [43], including OH, NO, NO_2, O, and O_3,

TABLE II
MEASURED GAS TEMPERATURE AND THE CORRESPONDING SPECTRAL BROADENINGS AT 5 slpm AND VARIOUS INPUT POWERS

Input Power	5 W	10 W	15 W
$T_g(K)$	315	330	350
$\Delta\lambda_{Stark}(nm)$	0.3	0.305	0.31
$\Delta\lambda_D(nm)$	0.01025	0.0105	0.01081
$\Delta\lambda_{vdW}(nm)$	0.04315	0.04177	0.04008

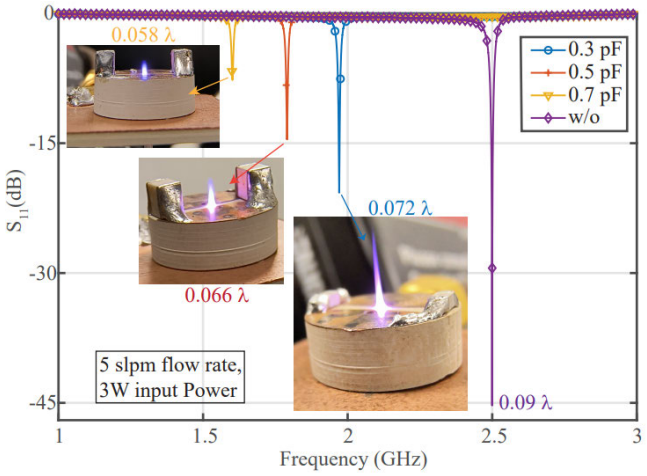

Fig. 11. Frequency tuning of the anapole plasma jet is realized by employing two tuning capacitors positioned at the edges of the tapered slots. By varying the capacitance within the range of 0.3–0.7 pF, the system achieves an impressive tuning capability, spanning nearly 900 MHz, with frequencies ranging from 2.5 GHz (no capacitor) to 1.6 GHz in the presence of the 0.7-pF capacitors.

among others. These reactive species have garnered considerable interest for their applicability in medical and agricultural contexts. The production of these reactive species is intricately linked to the specific attributes of the plasma jet, such as the background gas composition, the rate of gas flow, and the method employed to generate the plasma jet. For example, as demonstrated in [44], microwave plasma jets can yield substantial quantities of desirable NO species. The frequency of operation plays a pivotal role in influencing the production of a diverse array of reactive species. However, it is essential to note that the characteristics associated with frequency remain underexplored, mainly owing to the complex nature of microwave plasma jet technologies. Recent developments in low-power operated plasma jets [34], [35], [37] have significantly enhanced the accessibility of plasma sources for generating and utilizing reactive species within the microwave frequency range. However, these technologies are primarily built around cavities with electric fields confined within metallic enclosures, making frequency-tunable operations complex.

The presented anapole structure is designed as an open cavity featuring an accessible electric field for frequency tunability. As depicted in Fig. 11, this tunability is achieved by using two capacitors positioned at the edges of a tapered slot on the dielectric disk. This design facilitates tunable operation within a broad frequency range, spanning from 1.6 to 2.5 GHz, offering a 900-MHz bandwidth. To validate this concept, three prototypes were successfully demonstrated, each operating at different frequencies: 1.6, 1.8, and 1.97 GHz. In each case, a plasma jet was generated using a 5-slpm flow rate of helium with only 3 W of input power, highlighting the low-power operation of the system. Furthermore, adjusting the same design to a lower frequency of 1.6 GHz while maintaining the exact dimensions emphasizes its compactness, enabling scalability and facilitating seamless integration with microwave sources.

V. CONCLUSION

This work successfully demonstrated a novel, fully planar, compact, and frequency-tunable atmospheric pressure plasma jet device. This plasma jet technology leverages the capabilities of a dielectric anapole structure, a nonradiating resonator, to enhance the near electric field while effectively suppressing far-field radiation. This demonstration represents a pivotal step in unlocking a new pathway toward highly efficient plasma sources characterized by minimal reflection and radiation. The key advantages of the proposed technology, including its high electron density, compact form factor, seamless integration capability, and cost-effectiveness, hold the potential to open up new horizons for discovery and application. Given the profound impact of plasma technology across many fields, these advanced attributes are positioned to make substantial contributions to progress in various domains. Moreover, the inherent ease of frequency tunability of the proposed technology holds the promise of facilitating explorations into enriched chemistry within the RF/microwave spectrum, further enhancing its utility and versatility.

REFERENCES

[1] C. W. Hsu, B. Zhen, A. D. Stone, J. D. Joannopoulos, and M. Soljačić, "Bound states in the continuum," *Nat. Rev. Mater.*, vol. 1, no. 9, pp. 1–13, 2016.
[2] B. Luk'yanchuk et al., "The Fano resonance in plasmonic nanostructures and metamaterials," *Nature Mater.*, vol. 9, no. 9, pp. 707–715, Sep. 2010.
[3] F. Monticone and A. Alù, "Embedded photonic eigenvalues in 3D nanostructures," *Phys. Rev. Lett.*, vol. 112, no. 21, May 2014, Art. no. 213903.
[4] C. W. Hsu et al., "Observation of trapped light within the radiation continuum," *Nature*, vol. 499, no. 7457, pp. 188–191, Jul. 2013.
[5] X. Zhang and T. J. Cui, "Deep-subwavelength and high-Q trapped mode induced by symmetry-broken in toroidal plasmonic resonator," *IEEE Trans. Antennas Propag.*, vol. 69, no. 4, pp. 2122–2129, Apr. 2021.
[6] E. Zanganeh et al., "Nonradiating sources for efficient wireless power transfer," *Nanophotonics*, vol. 10, no. 17, pp. 4399–4408, Nov. 2021.
[7] A. Alù and N. Engheta, "Multifrequency optical invisibility cloak with layered plasmonic shells," *Phys. Rev. Lett.*, vol. 100, no. 11, Mar. 2008, Art. no. 113901.
[8] A. Alù and N. Engheta, "Cloaked near-field scanning optical microscope tip for noninvasive near-field imaging," *Phys. Rev. Lett.*, vol. 105, no. 26, Dec. 2010, Art. no. 263906.
[9] C. Zhang et al., "Terahertz meta-biosensor based on high-Q electrical resonance enhanced by the interference of toroidal dipole," *Biosensors Bioelectron.*, vol. 214, Oct. 2022, Art. no. 114493.
[10] S. B. Cohn, "Microwave bandpass filters containing high-Q dielectric resonators," *IEEE Trans. Microw. Theory Techn.*, vol. MTT-16, no. 4, pp. 218–227, Apr. 1968.
[11] F. S. Cuesta et al., "Nonscattering metasurface-bound cavities for field localization, enhancement, and suppression," *IEEE Trans. Antennas Propag.*, vol. 68, no. 3, pp. 1689–1703, Mar. 2020.
[12] T. Kaelberer, V. A. Fedotov, N. Papasimakis, D. P. Tsai, and N. I. Zheludev, "Toroidal dipolar response in a metamaterial," *Science*, vol. 330, no. 6010, pp. 1510–1512, Dec. 2010.
[13] V. A. Fedotov, A. V. Rogacheva, V. Savinov, D. P. Tsai, and N. I. Zheludev, "Resonant transparency and non-trivial non-radiating excitations in toroidal metamaterials," *Sci. Rep.*, vol. 3, no. 1, p. 2967, Oct. 2013.

[14] Y. Yang and S. I. Bozhevolnyi, "Nonradiating anapole states in nanophotonics: From fundamentals to applications," *Nanotechnology*, vol. 30, no. 20, May 2019, Art. no. 204001.

[15] J. R. Zurita-Sánchez, "Anapole arising from a mie scatterer with dipole excitation," *Phys. Rev. Res.*, vol. 1, no. 3, Oct. 2019, Art. no. 033064.

[16] A. E. Miroshnichenko et al., "Nonradiating anapole modes in dielectric nanoparticles," *Nature Commun.*, vol. 6, no. 1, p. 8069, Aug. 2015.

[17] U. Dey, S. Agasti, Y. Li, and J. Hesselbarth, "Analysis of anapole states in dielectric spheres and application to near-field enhancement," *IEEE Trans. Antennas Propag.*, vol. 70, no. 2, pp. 1144–1156, Feb. 2022.

[18] N. A. Nemkov, I. V. Stenishchev, and A. A. Basharin, "Nontrivial nonradiating all-dielectric anapole," *Sci. Rep.*, vol. 7, no. 1, p. 1064, Apr. 2017.

[19] E. Zanganeh, A. Evlyukhin, A. Miroshnichenko, M. Song, E. Nenasheva, and P. Kapitanova, "Anapole meta-atoms: Nonradiating electric and magnetic sources," *Phys. Rev. Lett.*, vol. 127, no. 9, Aug. 2021, Art. no. 096804.

[20] M. R. Akram and A. Semnani, "A microwave anapole source based on electric dipole interactions over a low-index dielectric," 2023, *arXiv:2308.15554*.

[21] M. Laroussi, "Low-temperature plasma jet for biomedical applications: A review," *IEEE Trans. Plasma Sci.*, vol. 43, no. 3, pp. 703–712, Mar. 2015.

[22] O. V. Penkov, M. Khadem, W.-S. Lim, and D.-E. Kim, "A review of recent applications of atmospheric pressure plasma jets for materials processing," *J. Coatings Technol. Res.*, vol. 12, no. 2, pp. 225–235, Mar. 2015.

[23] M. Ito, J. Oh, T. Ohta, M. Shiratani, and M. Hori, "Current status and future prospects of agricultural applications using atmospheric-pressure plasma technologies," *Plasma Processes Polym.*, vol. 15, no. 2, Feb. 2018, Art. no. 1700073.

[24] R. Betti and O. Hurricane, "Inertial-confinement fusion with lasers," *Nat. Phys.*, vol. 12, no. 5, pp. 435–448, 2016.

[25] A. Semnani, S. O. Macheret, and D. Peroulis, "A high-power widely tunable limiter utilizing an evanescent-mode cavity resonator loaded with a gas discharge tube," *IEEE Trans. Plasma Sci.*, vol. 44, no. 12, pp. 3271–3280, Dec. 2016.

[26] A. Semnani, D. Peroulis, and S. O. Macheret, "Plasma-enabled tuning of a resonant RF circuit," *IEEE Trans. Plasma Sci.*, vol. 44, no. 8, pp. 1396–1404, Aug. 2016.

[27] L. Bárdos and H. Baránková, "Cold atmospheric plasma: Sources, processes, and applications," *Thin Solid Films*, vol. 518, no. 23, pp. 6705–6713, Sep. 2010.

[28] A. Sadeghfam, A. Sadeghi-Ahangar, A. Elgamal, and H. Heuermann, "Design and development of a novel self-igniting microwave plasma jet for industrial applications," in *IEEE MTT-S Int. Microw. Symp. Dig.*, Jun. 2019, pp. 63–66.

[29] Y. C. Hong, D. H. Shin, S. J. Lee, Y. J. Kim, B. J. Lee, and H. S. Uhm, "Generation of high-power torch plasma by a 915-MHz microwave system," *IEEE Trans. Plasma Sci.*, vol. 39, no. 10, pp. 1958–1962, Oct. 2011.

[30] A. Gulec, F. Bozduman, and A. M. Hala, "Atmospheric pressure 2.45-GHz microwave helium plasma," *IEEE Trans. Plasma Sci.*, vol. 43, no. 3, pp. 786–790, Mar. 2015.

[31] Z. Wang, G. Zhang, Q. Zhang, and Z. Jia, "A large-volume open-air microwave plasma based on parallel multislot rectangular waveguides," *IEEE Trans. Plasma Sci.*, vol. 40, no. 5, pp. 1380–1385, May 2012.

[32] H. Heuermann, S. Holtrup, A. Sadeghfam, M. Schmidt, R. Perkuhn, and T. Finger, "Various applications and background of 10–200W 2.45 GHz microplasmas," in *IEEE MTT-S Int. Microw. Symp. Dig.*, Jun. 2012, pp. 1–3.

[33] F. Iza and J. A. Hopwood, "Low-power microwave plasma source based on a microstrip split-ring resonator," *IEEE Trans. Plasma Sci.*, vol. 31, no. 4, pp. 782–787, Aug. 2003.

[34] A. Semnani and K. S. Kabir, "A highly efficient microwave plasma jet based on evanescent-mode cavity resonator technology," *IEEE Trans. Plasma Sci.*, vol. 50, no. 10, pp. 3516–3524, Oct. 2022.

[35] J. Choi, A. H. Mohamed, S. K. Kang, K. C. Woo, K. T. Kim, and J. K. Lee, "900-MHz nonthermal atmospheric pressure plasma jet for biomedical applications," *Plasma Processes Polym.*, vol. 7, nos. 3–4, pp. 258–263, Mar. 2010.

[36] C. Zhao et al., "Microwave atmospheric pressure plasma jet generated from substrate integrated waveguide resonator," *Plasma Processes Polym.*, vol. 20, no. 6, Jun. 2023, Art. no. e2200230.

[37] K. S. Kabir and A. Semnani, "A power-efficient microwave microplasma jet utilizing an SIW evanescent-mode cavity resonator," in *IEEE MTT-S Int. Microw. Symp. Dig.*, Jun. 2023, pp. 648–651.

[38] E. A. Gurvitz, K. S. Ladutenko, P. A. Dergachev, A. B. Evlyukhin, A. E. Miroshnichenko, and A. S. Shalin, "The high-order toroidal moments and anapole states in all-dielectric photonics," *Laser Photon. Rev.*, vol. 13, no. 5, 2019, Art. no. 1800266.

[39] P. J. Soh, G. Vandenbosch, F. H. Wee, A. van den Bosch, M. Martinez-Vazquez, and D. Schreurs, "Specific absorption rate (SAR) evaluation of textile antennas," *IEEE Antennas Propag. Mag.*, vol. 57, no. 2, pp. 229–240, Apr. 2015.

[40] J. Gemio, J. Parron, and J. Soler, "Human body effects on implantable antennas for ism bands applications: Models comparison and propagation losses study," *Prog. Electromagn. Res.*, vol. 110, pp. 437–452, 2010.

[41] S. T. Lee, W. J. Nam, J. K. Lee, and G. S. Yun, "In situ impedance measurement of microwave atmospheric pressure plasma," *Plasma Sources Sci. Technol.*, vol. 26, no. 4, Mar. 2017, Art. no. 045004.

[42] N. Srivastava and C. Wang, "Effect of N_2 and O_2 on OH radical production in an atmospheric helium microwave plasma jet," *Plasma Sci. Technol.*, vol. 21, no. 11, Nov. 2019, Art. no. 115401.

[43] M. Keidar, "Adaptive low-temperature plasmas," *Plasma Phys. Controlled Fusion*, 2023.

[44] A. F. H. van Gessel, B. Hrycak, M. Jasiński, J. Mizeraczyk, J. van der Mullen, and P. J. Bruggeman, "Temperature and NO density measurements by LIF and OES on an atmospheric pressure plasma jet," *J. Phys. D, Appl. Phys.*, vol. 46, no. 9, Mar. 2013, Art. no. 095201.

Muhammad Rizwan Akram (Member, IEEE) received the B.E. degree in electronic engineering from GIK Institute, Topi, Pakistan, in 2013, the M.S. degree in information and communication engineering from Huazhong University of Science and Technology (HUST), Wuhan, China, in 2016, and the Ph.D. degree in electronic science and technology from Shanghai Jiao Tong University (SJTU), Shanghai, China, in 2021.

He has been a Post-Doctoral Researcher with The University of Toledo, Toledo, OH, USA, since November 2022. Before joining UToledo, he briefly worked as a Post-Doctoral Researcher at Nagoya Institute of Technology, Nagoya, Japan. From 2014 to 2016, he received Bi-Lateral Scholarship at HUST for his M.S. degree. From 2017 to 2021, he received CSC Scholarship at SJTU for his Ph.D. degree. His research interests include exploring wave–matter interaction within the electromagnetic spectrum, such as anapoles, electromagnetically induced transparency, Huygens' sources, and EM-plasma devices.

Dr. Akram received the 2024 IEEE AP-S Fellowship Award and the Excellent International Postgraduate Student Award 2021 at SJTU.

Abbas Semnani (Senior Member, IEEE) received the B.Sc. degree in electrical engineering from the University of Tehran, Tehran, Iran, in 2000, and the M.Sc. and Ph.D. degrees in electrical engineering from the K. N. Toosi University of Technology, Tehran, in 2002 and 2009, respectively.

He is currently an Associate Professor with the Department of Electrical Engineering and Computer Science, The University of Toledo, Toledo, OH, USA. Before joining UToledo in 2019, he was at Purdue University, West Lafayette, IN, USA, where he has been specialized in plasma–electromagnetic interactions and plasma for high-power radio frequency tuning, since 2012. Prior to that, he was a Research and Teaching Associate at the Department of Electrical and Computer Engineering, K. N. Toosi University of Technology, from 2009 to 2012. During the Ph.D. degree, he had a Visiting Scholarship at the Aristotle University of Thessaloniki, Thessaloniki, Greece, in 2008, focusing on novel computational techniques for solving time-domain inverse scattering problems. His current research interests encompass high-power microwaves, low-temperature plasmas, reconfigurable RF electronics, and tunable and small antennas.

Dr. Semnani received the 2019 IEEE MTT-S "Tatsuo Itoh" Award, the NASA Glenn Faculty Fellowship in 2022, and the NSF CAREER Award in 2024.